Available online at www.sciencedirect.com
SCIENCE DIRECT®
International Journal of Heat and Mass Transfer 48 (2005) 511–525
International Journal of HEAT and MASS TRANSFER
www.elsevier.com/locate/ijhmt

Effects of jet-to-disk separation distance on the characteristics of mixed convective vortex flow in an impinging air jet confined in a cylindrical chamber

J.C. Hsieh, T.F. Lin *

Department of Mechanical Engineering, National Chiao Tung University, Hsinchu, Taiwan 30010, ROC

Received 23 January 2004; received in revised form 10 September 2004
Available online 11 November 2004

Abstract

How the jet-to-disk separation distance H affects various aspects of the laminar mixed convective vortex flow resulting from a low speed air jet impinging onto a heated horizontal disk confined in a vertical adiabatic cylindrical chamber is explored herein by flow visualization combined with temperature measurement. In the present study the air flow rate is varied from 1.0 to 8.0 slpm (standard liter per minute) for two different injection pipes with the temperature difference between the heated disk and air injected into the chamber varied from 0 to 25.0 °C at four jet-to-disk separation distances. The corresponding jet Reynolds and Rayleigh numbers, respectively, range from 0 to 1082 and from 0 to 63,420. The experimental results clearly reveal a new vortex roll. More specifically, in the upper range of the jet Reynolds number tested here a small tertiary inertia-driven circular vortex roll appears near the upper wall of the chamber, in addition to the previously known primary and secondary inertia-driven rolls. Besides, we also note that a reduction in the jet-to-disk separation distance causes a delayed onset of the inertia-driven rolls except for $H \geqq 20.0$ mm and in the meantime causes a substantial decrease in the Rayleigh number since $Ra \propto H^3$, which in turn significantly reduces the size and strength of the buoyancy-driven roll. Moreover, the inertia-driven rolls are bigger for a larger H. At the largest H (=30.0 mm) tested here both the primary inertia-driven roll and buoyancy-driven roll are relatively large and they can contact with each other. Hence no space is available for the secondary inertia-driven roll to appear. Our data also suggest that the onset of the buoyancy roll takes place when the local buoyancy-to-inertia ratio at the edge of the disk $Gr/Re_{we}^2 \approx 33.0$ within the experimental uncertainty. Finally, the temperature data indicate that the steady radial air temperature distributions are non-monotonic which mainly reflects the counter-rotating vortex flow structure of the primary inertia-driven and buoyancy-driven rolls.

1. Introduction

Fluid flow and heat transfer associated with jets impinging onto heated surfaces have been extensively studied over the past due to their superior heat removal capability. The results [1] have been applied to improve the drying of textiles and paper, annealing of glass,

* Corresponding author. Tel.: +886 35 712121x55118; fax: +886 35 726 6440.
E-mail address: tflin@mail.nctu.edu.tw (T.F. Lin).

0017-9310/$ - see front matter © 2004 Elsevier Ltd. All rights reserved.
doi:10.1016/j.ijheatmasstransfer.2004.09.014

Nomenclature

D_j	jet diameter at the injection pipe exit (mm)
G	gravitational acceleration (m/s^2)
Gr	Grashof number, $g\beta\Delta TH^3/v^2$
Gr/Re_j^2	critical buoyancy-to-inertia ratio for the onset of buoyancy induced roll
H	distance between the exit of injection pipe and heated plate (mm)
Q_j	jet flow rate (standard liter per minute, slpm)
r_s	the center of the location of secondary inertia-driven roll (mm)
r, θ, z	dimensional cylindrical coordinates
R, Θ, Z	dimensionless cylindrical coordinates, r/R_C, θ, z/H
R_C	radius of processing chamber (mm)
Ra	Rayleigh number, $g\beta\Delta TH^3/\alpha v$
Re_j	jet Reynolds number, $\overline{V_j}D_j/v$
Re_w	local Reynolds number in the wall-jet region, $\overline{u}H/v$
Re_{we}	local Reynolds number in the wall-jet region at the edge of heated disk
S_I	size of primary inertia-driven roll in radial direction (mm)
S_O	size of buoyancy-driven roll in axial direction (mm)
T_f	temperature of the heated disk (°C)
T_j	temperature of jet at the injection pipe exit (°C)
$\overline{u}$	average radial velocity of the flow at wall-jet region (m/s), $(Re_jD_jv)/(8rH)$
$\overline{V_j}$	average axial velocity of the air jet at the injection pipe exit (m/s)

Greek symbols

α	thermal diffusivity (cm^2/s)
β	thermal expansion coefficient (1/K)
ΔT	temperature difference between the heated disk and the injected air (°C)
v	kinematic viscosity (cm^2/s)
Φ	non-dimensional temperature, $(T - T_j)/(T_f - T_j)$

cooling of gas turbine components and microelectronic equipments, freezing of tissue in cryosurgery, etc. In these applications high speed jets are normally employed and the resulting flow is forced convection dominated with negligible buoyancy effects. Some vortex flow driven by the jet inertia due to the jet entrainment has been observed. However, for application such as the growth of thin crystal films from the chemical vapor deposition (CVD) processes [2–4], the radial uniformity of heat and mass transfer rate on the heated surfaces is of major concern and the jets no longer move at high speeds. Thus the buoyancy effects in the flow cannot be ignored. Besides, the flow needs to be stable and contain no vortices. The interest in the impinging jet confined in a chamber accelerates recently because the presence of the flow recirculation in the processing chamber is detrimental to the film properties. In an attempt to examine the flow recirculation in an impinging gas jet we recently visualized the vortex flow in a model processing chamber with a fixed jet-to-plate separation distance $H = 20.0$ mm [5] and found that the flow was dominated by the circular vortex rolls driven by the jet inertia and buoyancy force. More specifically, two circular rolls are often driven by the jet inertia which is designated as the primary and secondary inertia-driven rolls. Moreover, the buoyancy force induces a circular roll near the chamber side. In this study we move further to investigate the effects of the jet-to-disk separation distance on various characteristics of the vortex flow in a low speed mixed convective gas jet impinging onto a heated plate. Particularly, the critical conditions for the onset of and the steady-unsteady transition of the inertia and buoyancy-driven rolls and the steady vortex flow characteristics affected by the jet-to-disk separation distance will be delineated. Besides, the possible presence of the tertiary inertia-driven rolls will be explored.

Considerable amount of work has been carried out in the past to study the fluid flow and heat transfer in the round or slot jet impinging onto a large horizontal plate without any confinement. Most of the studies focused on quantifying the highly efficient heat transfer associated with the high speed impinging jets. For instances, heat or mass transfer in the impinging jets over a large plate was experimentally investigated by Scholtz and Trass [6], Sparrow and Wong [7], Masliyah and Nguyen [8], and Hrycak [9]. The laminar impinging jets with an upper plate confinement were numerically predicted by Saad et al. [10] and Law and Masliyah [11]. A pair of big flow recirculations around the jet axis were noted to be induced by a confinement plate above the target plate [12,13]. The characteristics of the recirculations were found to be determined by the jet Reynolds number Re_j and nozzle-to-plate spacing H [14,15]. Their numerical results revealed that the center of the flow recirculation moved away from the jet axis at increasing H. Moreover, the secondary flow in a confined impinging jet consists of a large recirculation vortex around the jet axis and a comparatively smaller adjacent second-

ary vortex right above the impinging plate (Law and Masliyah [11,16]). More recently, for a confined laminar impinging jet ($Re_j < 1000$) the critical jet Reynolds number for the onset of unsteady flow was numerically shown to be between 585 and 610 [17]. The unsteady jet was characterized by a dominant frequency corresponding to the formation of shear layer vortices at the jet exit. More complete information on the impinging jets can be found from the critical reviews conducted by Viskanta [18] and Jambunathan et al. [19].

In the impinging jet flow confined in a chamber encountered in the CVD, the gases input to the CVD chamber are at relatively low flow rates and the wafer upon which thin crystal films are grown and processed is at an elevated temperature with the Reynolds and Rayleigh numbers, respectively, ranging from 1.0 to 100 and from 0 to 10^5 [4]. Under such circumstance the buoyancy in the flow is no longer small compared with the jet inertia. Significant flow recirculation can be induced by the combined effects of the inertia and buoyancy. The importance of the buoyancy on the recirculating flow in a vertical CVD reactor was demonstrated by Wahl [20]. Similar investigations have been carried out for various types of CVD reactors including the metal organic CVD [21–23]. In these studies for the processing of the microelectronic circuits [20–23] various vortex flow patterns were reported in the jet impinging flow. Buoyancy induced symmetry breaking of the jet flow was also noted [23].

The above literature review clearly reveals that how the jet-to-disk separation distance affects the detailed vortex flow characteristics in a mixed convective low speed gas jet impinging onto a heated plate in a confined chamber in which both inertia and buoyancy-driven flow recirculations are significant remains poorly understood. An experiment combining flow visualization and temperature measurement is conducted here to investigate the effects of the jet-to-disk separation distance on various aspects of the low speed impinging jet flow.

2. Experimental apparatus and procedures

In order to conduct the experiment at reasonably low cost, we use air as the working fluid in the present experiment to replace the inert gases normally employed in real CVD processes. In view of the similar thermodynamic and thermophysical properties for various gases, the results obtained here are still applicable to the CVD system. The experimental system established in our previous study [5] is employed here to investigate the effects of the jet-to-plate distance on the vortex flow characteristics associated with a round jet impinging vertically downwards onto a circular heated horizontal disk confined in a vertical cylindrical chamber. Schematics of the experimental system and test section are, respectively, shown in Figs. 1 and 2. The system consists of four major parts the processing chamber, temperature measurement and data acquisition unit, heating unit, and gas injection unit. The major parts are briefly described in the following.

The processing chamber is made of 6.0-mm thick quartz glass to allow for the observation of the vortex flow in it. The chamber is cylindrical and has a diameter of 291.0 mm and the height of the cylindrical chamber is 200.0 mm. To facilitate the flow visualization, the chamber top is made of an acrylic plate. Air is injected vertically downward from a long straight circular pipe into the cylindrical chamber along the axis of the chamber and impinges directly onto the heated disk. The air first flows over the heated disk, then moves through the annular section of the chamber, and finally leaves the chamber via twenty circular outlets of 12.7 mm in diameter opened at the bottom of chamber. The chamber is sealed to prevent any gas leakage. The top, bottom and side walls of the chamber are thermally well insulated to reduce the heat loss from the processing chamber to the ambient by covering the entire chamber with a superlon insulator of 100.0-mm thick. The insulator can be opened during the flow visualization.

The heating unit is designed to maintain the circular disk at the preset uniform temperature during the experiment. It is composed of a 25.0-mm thick high purity circular copper plate of 8 in. in diameter, acting as the disk. The heater attached onto the back side of the copper plate is divided into three concentric zones. Each zone is independently heated by a D.C. power supply with D.C. current passing through the nickel coil placed on a stainless steel base. To reduce the heat loss from the sidewall of the copper plate and stainless steel base, the lateral surface of the entire heating unit is wrapped with a 16-mm thick thermal insulation layer of superlon. Care is taken to insure that the outside surface of the insulation layer is smooth and cylindrical. The entire heating unit is then placed on a Teflon plate. A proper control of the voltage from each power supply allows us to maintain the copper plate at a nearly uniform temperature. The measured data indicate that the uncertainty in maintaining the copper plate temperature is ±0.1 °C. No bias in the plate temperature is noted and the temperature non-uniformity is spatially random.

The gas injection unit consists of a 2HP air compressor, a flow meter, a smoke generator, filters, pressure regulator, and connection and injection pipes. In the experiments, air is drawn from the ambient by the compressor and sent into a 300-l and 100-psi high-pressure air tank and is filtered to remove moisture and tiny particles. The installation of the high-pressure air tank intends to suppress the fluctuation of the air flow and extends the life of the compressor. Then, the air is mixed with smoke tracers in the smoke generator and regulated by the pressure regulator, and is later injected into the

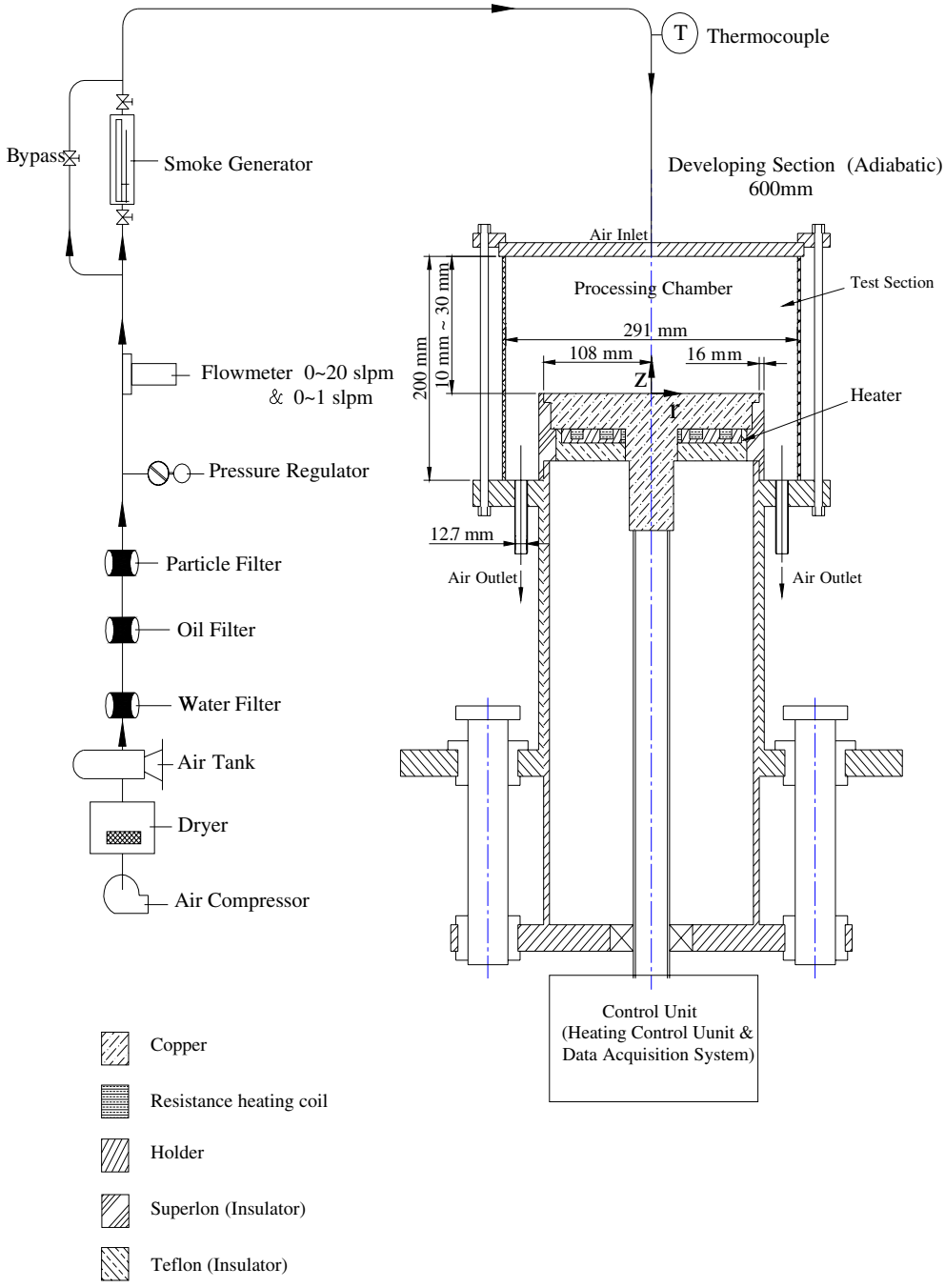

Fig. 1. Schematic diagram of the experimental system.

processing chamber through the straight circular injection pipe which is coaxial with the processing chamber. The downward vertical air jet issuing from the pipe exit impinges directly onto the heated plate. In the present study, two injection pipes with diameter 10.0 mm and 22.1 mm are tested and the straight portions of the pipes are both 600.0 mm long. This length of the injection pipes is selected to ensure that they are long enough for the flow to become fully developed in the pipes. The separation distance between the exit of the injection pipe and the heated disk is chosen to be 10.0, 15.0, 20.0 and 30.0 mm. The air temperature at 600.0 mm upstream

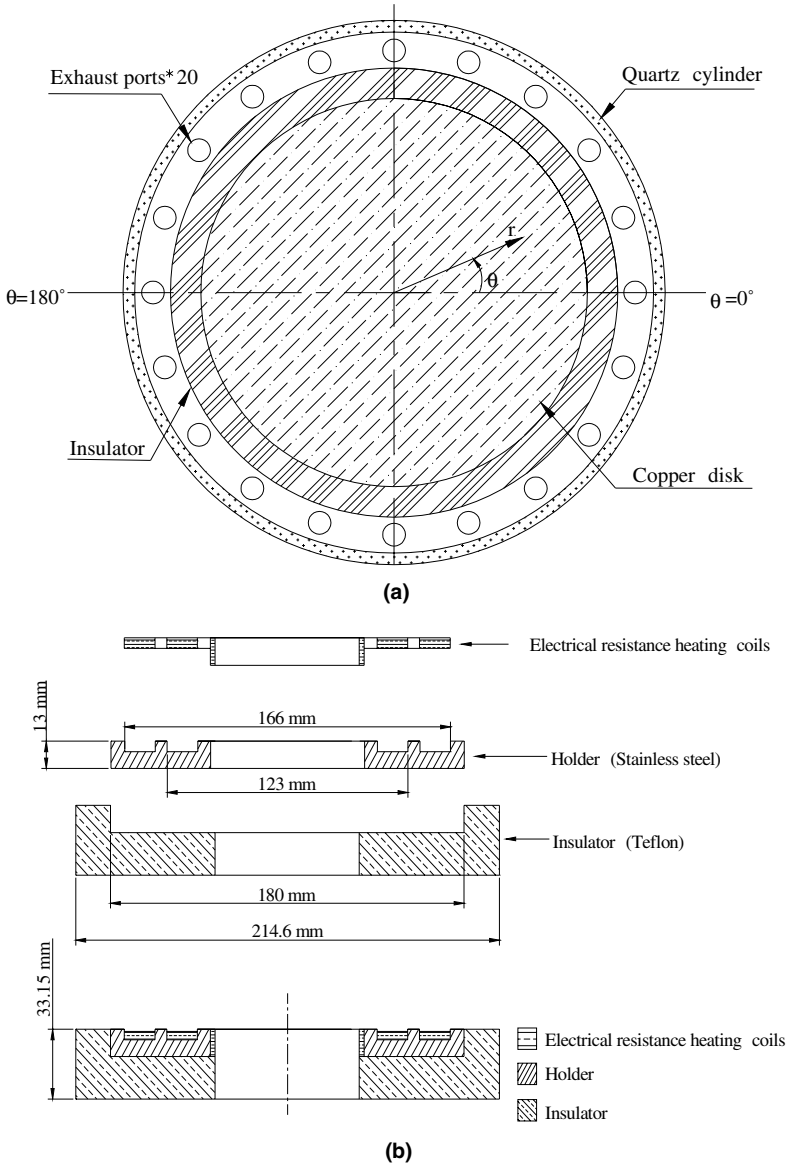

Fig. 2. Schematic of (a) the test section from the top view and (b) 3-zone concentric heater.

of the exit of the injection pipe is measured by a corrected and calibrated T-type thermocouple. The measured value is considered as the temperature of the air injected into the processing chamber since the whole injection pipe is thermally well insulated by a 16.0 mm layer of superlon insulation.

A smoke-tracer flow visualization technique is employed to observe the flow patterns in the cylindrical chamber. The gas flow pattern is illuminated by the vertical and horizontal plane light sheets produced by passing parallel light sheets from an overhead projector through adjustable knife edges. The experimental system is located in a darkroom to improve the contrast of the flow photos. The time variations of the flow pattern during the entire transient stage from the top and side views are recorded by the Sony digital video camera DCR-PC100. The recorded images are later examined carefully in a personal computer. The air temperature in the processing chamber is measured by inserting a small thermocouple probe into the chamber through small holes of 1.0 mm in diameter opened at the top of the chamber. The probe is an OMEGA (model HYPO) mini hypodermic extremely small T-type thermocouple implanted in a 1 in. long stainless steel hypodermic needle.

For each case the experiment starts with the air at the room temperature compressed first into the smoke

generator through the connection pipe and then injected into the processing chamber. The air moves over the heated disk and finally leaves the chamber through the outlets at the bottom of the chamber. In the meantime the temperature of the disk and the air flow rate are controlled at the preset levels. As the mixed convective air flow in the processing chamber reaches steady or statistically stable state, we begin to visualize the vortex flow pattern in the chamber.

Uncertainties in the Rayleigh number, Reynolds number and other independent parameters are calculated according to the standard procedures established by Kline and McClintock [24]. The uncertainties of the thermophysical properties of the air are also included in the analysis. The properties of the working fluid (air) are $\alpha = 0.22$ (cm^2/s), $\beta = 0.0034$ (1/K), $\nu = 0.16$ (cm^2/s) and $Pr = 0.72$ at 30 °C and 1.0 bar. In addition, the uncertainties of the control unsteadiness and temperature non-uniformity are accounted for in the evaluation of the data uncertainty. The analysis shows that the uncertainties of temperature, volume flow rate, dimensions, Reynolds number and Rayleigh number measurements are estimated to be less than ±0.2 °C, ±2%, ±0.05 mm, 2.3% and 8.6%, respectively.

To validate our experimental setup, the flow observed in the processing chamber for the limiting case when the disk is unheated ($Ra = 0$) is compared with the numerical results from Law and Masliyah [11] for the impinging jet flow with top plate confinement but without the sidewall confinement. It is noted that in the region surrounding the jet axis the resulting vortex flow from our flow visualization is nearly the same as their numerical prediction. Thus, the experimental system established here is considered to be suitable for the present study.

3. Results and discussion

In the present experiment two injection pipes of diameter $D_j = 10.0$ and 22.1 mm are used. The jet flow rate Q_j and jet-to-disk temperature difference ΔT are, respectively, varied from 1.0 to 8.0 standard liter per minute (slpm) and from 0 to 25.0 °C with the jet-to-disk separation distance H varied from 10.0 to 30.0 mm. The corresponding jet Reynolds number $Re_j (= \overline{V}_j D_j/\nu = 4Q_j/\pi\nu D_j)$ ranges from 61 to 1082 and Rayleigh number Ra ($=g\beta\Delta TH^3/\alpha\nu$) from 0 to 63,420. The associated Grashof number Gr ($=Ra/Pr$) ranges from 0 to 88,080. In addition, the local Reynolds number and average radial velocity of the flow in the wall-jet region are, respectively, defined as

$$Re_w = \bar{u}H/\nu \tag{1}$$

and

$$\bar{u} = Q_j/2\pi rH = Re_j D_j \nu/(8rH) \tag{2}$$

Hence Re_w can be rewritten as

$$Re_w = Re_j \cdot D_j/8r \tag{3}$$

Selected results from our flow visualization and measured air temperature are presented in the following to illustrate the effects of the jet-to-disk separation distance on various aspects of the vortex flow characteristics in the chamber.

3.1. Onset of the vortex rolls

At first, the effects of the jet-to-disk separation distance on the critical conditions for the appearance of the inertia and buoyancy-driven vortex rolls are examined. The critical Re_j for the onset of the inertia-driven rolls is located by directly visualizing the flow at which the rolls start to appear for an unheated disk ($\Delta T = 0$ °C) at various H. The procedures were detailed in the earlier study [5]. Some flow photos near the critical condition for the onset of the primary and secondary inertia-driven rolls for $H = 20.0$ mm are already given there. Note that the lowest jet flow rate which can be accurately resolved in the present experimental apparatus is 0.1 slpm. Even at this small Q_j the primary inertia-driven roll is already seen in the chamber for all H with the jet issued from the small injection pipe

Table 1
Critical condition for appearance of the inertia-driven vortex rolls ($\Delta T = 0$ °C)

Vortex Roll	Separation distance (H, mm)	Jet diameter (D_j, mm)	Flow rate (Q_j, slpm)	Gr	Re_j
Primary inertia-driven roll	30.0	22.1	0.25	0	15
	20.0	22.1	0.25	0	15
	15.0	22.1	0.3	0	18
	10.0	22.1	0.7	0	43
Secondary inertia-driven roll	30.0	10.0	0.8	0	108
		22.1	3.3	0	202
	20.0	10.0	1.3	0	180
		22.1	3.6	0	220
	15.0	10.0	1.7	0	230
		22.1	4.9	0	300
	10.0	10.0	1.8	0	245
		22.1	7.0	0	430
Tertiary inertia-driven roll	30.0	10.0	5	0	676
	20.0	10.0	5	0	676
	15.0	10.0	5.5	0	744
	10.0	10.0	7	0	947

(D_j = 10.0 mm). For the large injection pipe (D_j = 22.1 mm) the critical Re_j for the onset of the primary inertia-driven roll is somewhat higher and thus can be located here. The present data are summarized in Table 1 for the onset of the primary and secondary inertia-driven rolls at various jet-to-disk separation distances. Besides, the onset conditions of the tertiary inertia-driven roll are also given in the table. The characteristics of the tertiary roll will be inspected later.

The results given in Table 1 indicate that at given D_j the critical jet Reynolds numbers for the onset of the primary, secondary and tertiary inertia-driven rolls increase when the jet-to-disk separation distance is reduced from 20.0 mm to 10.0 mm. However, it is of interest to note that the critical Re_j does not experience any change when H is reduced from 30.0 to 20.0 mm for the primary and tertiary rolls. The increase of the critical Re_j at decreasing H is conjectured to mainly result from the more significant retarding of the jet by the disk at a smaller H, which, in turn, yields a higher viscous damping effect on the impinging jet and a higher Re_j is needed to induce the flow recirculations. We also note that at somewhat higher Re_j a tertiary roll can appear in the chamber for D_j = 10.0 mm. For D_j = 22.1 mm the range of the jet Reynolds number covered in the present study is not high enough to induce a tertiary roll.

The inertia-driven steady tertiary flow is illustrated in Fig. 3 by showing the steady side view flow photos taken at the cross plane $\theta = 0°$ for slightly supercritical jet Reynolds numbers at various jet-to-disk separation distances for D_j = 10.0 mm. Since the steady flow is axisymmetric, only the results in the half plane are shown. The

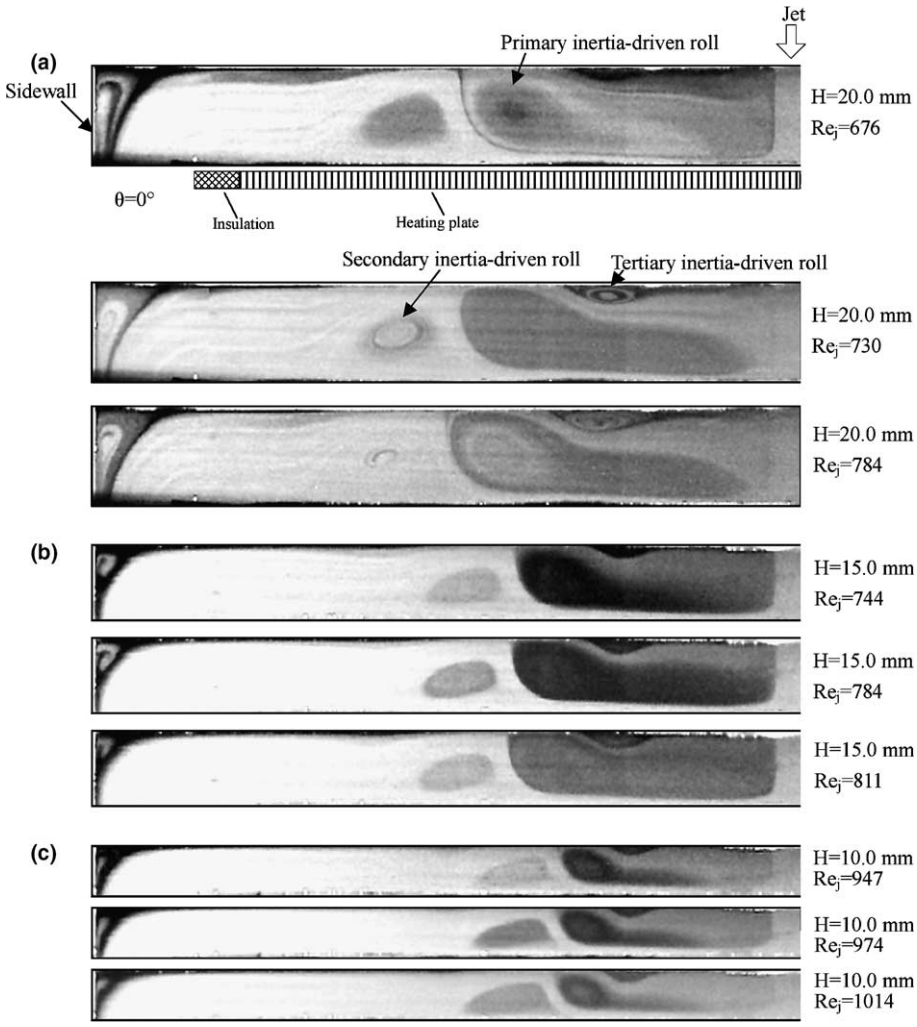

Fig. 3. Steady side view flow photos taken at the cross plane $\theta = 0°$ for various Re_j to illustrate the tertiary inertia-driven roll with $Ra = 0$ and D_j = 10.0 mm for (a) H = 20.0 mm, (b) H = 15.0 mm and (c) H = 10.0 mm.

results in Fig. 3 manifest that the tertiary roll is small and appears in the region near the chamber top adjacent to the primary inertia-driven roll. As the primary and secondary rolls, the tertiary roll is smaller at the smaller jet-to-disk separation distance. This simply reflects the fact that at a smaller H the available space in the processing chamber for the rolls to develop is less. Note that at $H = 10.0$ mm the tertiary roll is rather small. Besides, the tertiary roll grows slightly in size and in vortex intensity with the jet Reynolds number. At the larger jet-to-disk separation distance for $H = 20.0$ mm the growth of the tertiary roll with Re_j is slightly larger, as evident from the results in Fig. 3(a). Moreover, the tertiary roll becomes smaller and weaker for an increase in Ra. A close inspection of the successive side view flow photos stored in the video tapes during the transient stage for the formation of the inertia-driven rolls reveals that at increasing Re_j the primary roll gets larger and stronger. At certain high Re_j the primary roll is strong enough to induce a tertiary roll through the viscous shearing of the stagnant flow around the primary roll.

As we continue to increase the jet Reynolds number slightly beyond the critical Re_j for the onset of the tertiary roll, the flow in the processing chamber does not reach any steady state at long time. Instead, the flow becomes time dependent and experiences a transition from steady to unsteady states. Obviously, this transition is driven by the jet inertia since $\Delta T = 0\,^{\circ}C$. The present data for the inertia-driven steady-to-unsteady transition are summarized in Table 2 for $D_j = 10.0$ mm. The results indicate that the critical Re_j for this flow transition increases when the jet-to-disk separation distance is shortened, similar to those for onset of the inertia-driven rolls.

When the disk is heated, our flow visualization further shows that for given D_j, ΔT and H the buoyancy-driven roll begins to appear in the region near the heated disk edge as Re_j is below certain critical level for a given Ra. This critical condition is considered to be reached as long as we can barely see the buoyancy-driven roll in the video films recording the images of the vortex rolls [5]. Table 3 summarizes the critical condition for the onset of the buoyancy-driven roll based on the present data. The data indicate that for given D_j and H the critical Re_j for the onset of the buoyancy-driven roll is higher for a higher Gr. It should be mentioned that how the onset condition of the buoyancy roll is affected by the jet-to-disk separation distance is reflected in the Grashof number since Gr is proportional to H^3. Note that the critical buoyancy-to-inertia ratio Gr/Re_j^2 for the onset of the buoyancy roll is nearly constant for a given D_j, irrespective of the jet-to-disk separation distance. For $D_j = 10.0$ and 22.1 mm the critical ratio Gr/Re_j^2 is nearly equal to 0.0045 and 0.021, respectively. It is also noted that the onset of the buoyancy-driven roll occurs when the wall-jet flow in the radial direction is reversed by the upward buoyancy associated with the heated disk and hence the onset should be mainly determined by the local flow condition characterized by the local Reynolds number of the wall-jet flow Re_w and the Grashof

Table 2
Critical condition for onset of time-dependent flow for unheated disk and $D_j = 10.0$ mm

H (mm)	D_j (mm)	ΔT (°C)	Q_j (slpm)	Re_j	Flow field
30.0	10.0	0	5.8	784	Steady
30.0	10.0	0	5.9	798	Unsteady
20.0	10.0	0	5.8	784	Steady
20.0	10.0	0	5.9	798	Unsteady
15.0	10.0	0	6.1	825	Steady
15.0	10.0	0	6.2	839	Unsteady
10.0	10.0	0	7.6	1028	Steady
10.0	10.0	0	7.7	1041	Unsteady

Table 3
Critical condition for onset of the buoyancy-driven vortex roll

Jet diameter (D_j, mm)	Separation distance (H, mm)	Gr	Re_j	Gr/Re_j^2	Gr/Re_{we}^2	Deviation (%)
10.0	20.0	3340	879	0.0043	32.3	2.2
		4200	947	0.0047	35.0	5.9
		5220	1082	0.0045	33.3	0.8
	15.0	1321	541	0.0045	33.7	2.0
		2202	676	0.0048	36.0	9.0
	10.0	1304	541	0.0044	33.3	0.8
		1957	676	0.0043	32.0	3.1
22.1	20.0	3340	398	0.021	32.2	2.5
		4200	459	0.020	30.5	7.7
		5220	520	0.019	29.5	10.7
	15.0	1321	245	0.022	33.7	2.0
		2202	306	0.024	35.9	8.7
	10.0	1304	245	0.022	33.2	0.5
		1957	306	0.021	31.9	3.4

number Gr. Besides, the onset is most likely to take place near the outer edge of the disk. This is indeed the case [5]. Therefore, the onset condition is expected to depend primarily on the local buoyancy-to-inertia ratio Gr/Re_w^2. The data given in Table 3 do show that the buoyancy roll begins to appear when the local buoyancy-to-inertia ratio at the edge of the disk Gr/Re_{we}^2 is around 33.0 for all D_j and H considered.

3.2. Characteristics of steady vortex rolls

According to the definitions of Re_j and Ra, the jet Reynolds number is independent of H but the Rayleigh number depends on H^3. Thus a change in the jet-to-disk separation distance is expected to exert profound influences on the buoyancy-driven vortex roll at supercritical Ra. Besides, it is of interest to inquire whether we can ignore the effects of H on the vortex flow driven by the jet inertia force. To illustrate the effects of the jet-to-disk separation distance on the steady vortex flow, Figs. 4–6 show steady side view flow photos taken at the cross plane $\theta = 0°$ and 180° for various H at selected Q_j and ΔT for both injection pipes. First, we note that for the unheated disk with $\Delta T = 0\,°C$ and at the same D_j and Q_j both the primary and the secondary inertia-driven rolls are significantly bigger for an increase in H (Fig. 4). The above results manifest that the jet-to-disk separation distance produces noticeable effects on the inertia-driven vortex flow and cannot be neglected. Additionally, for every H we have another circular vortex roll in the corner region

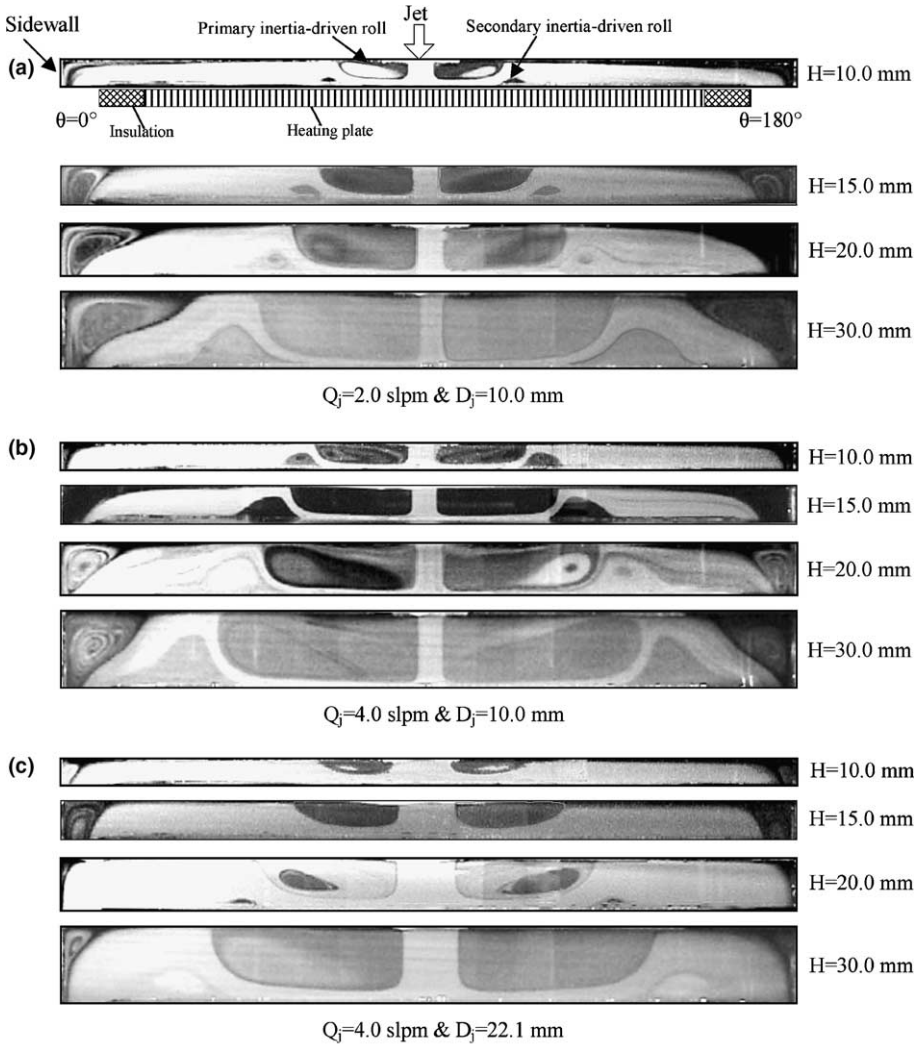

Fig. 4. Steady side view flow photos taken at the cross plane $\theta = 0°$ and 180° for $Ra = 0$ with (a) $Re_j = 270$ and $D_j = 10.0$ mm, (b) $Re_j = 541$ and $D_j = 10.0$ mm and (c) $Re_j = 245$ and $D_j = 22.1$ mm.

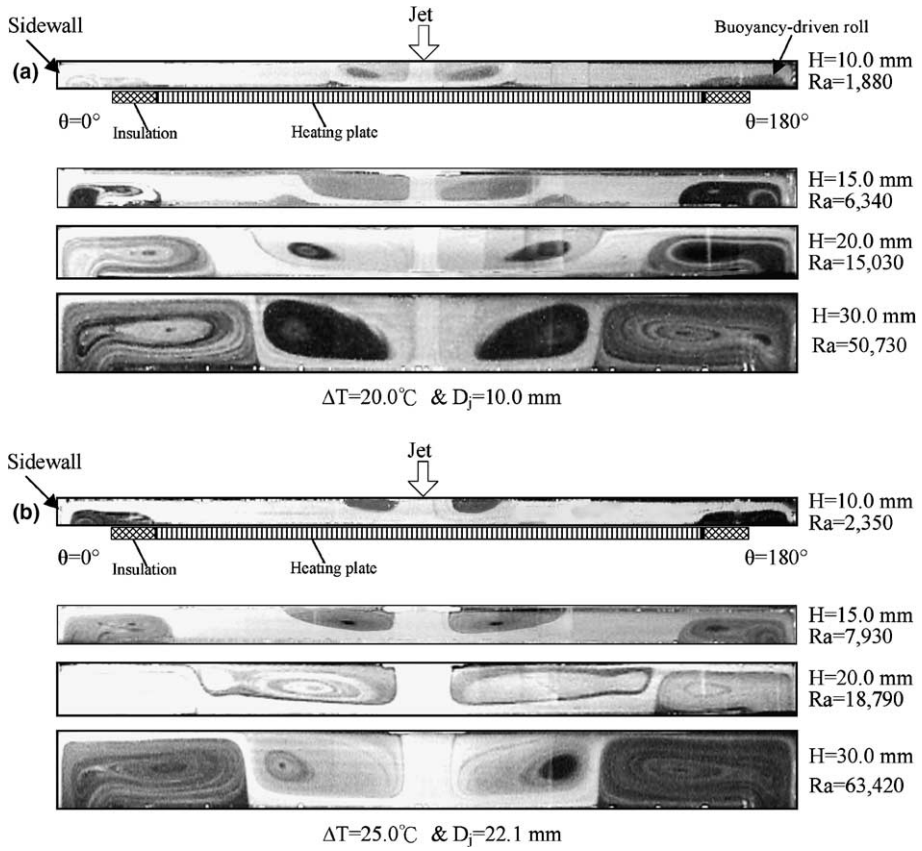

Fig. 5. Steady side view flow photos taken at the cross plane $\theta = 0°$ and 180° at various H with $Q_j = 2.0$ slpm for (a) $\Delta T = 20.0$ °C and $Re_j = 270$ and (b) $\Delta T = 25.0$ °C and $Re_j = 122$.

of the chamber except the primary and the secondary inertia-driven vortex rolls. This additional roll is not induced by the buoyancy because the disk is unheated and no buoyancy is present in the flow. In fact, this roll emerges from the deflection of the flow from the wall-jet by the chamber side and it is bigger at a higher jet-to-disk separation distance for $D_j = 10.0$ mm. However, the size change of the corner roll with the variation in Re_j is much smaller. Moreover, for large injection pipe ($D_j = 22.1$ mm) the corner roll is small and is insignificantly affected by the jet-to-disk separation distance (Fig. 4(c)).

Next, the effects of the jet-to-disk separation distance on the buoyancy-driven roll are exemplified in Fig. 5 by showing the steady side view flow photos for $Q_j = 2.0$ slpm and $\Delta T = 20.0$ °C and 25.0 °C at various H. The results clearly indicate that the buoyancy-driven vortex roll which dominates in outer region of the processing chamber is much bigger for a larger H. This large increase in the size of the buoyancy-driven roll with the jet-to-disk separation distance is due to the large increase in Ra associated with a small increase in H since Ra is proportional to H^3, as mentioned above. It is of interest to note that at the largest H (=30.0 mm) tested here the radial extent of the buoyancy-driven roll is so large and it directly contacts with the primary inertia-driven roll. Thus, no space is available for the secondary inertia-driven roll to emerge. Only two circular vortex rolls appear in the chamber for $H = 30.0$ mm.

Then, how the jet-to-disk temperature difference ΔT affects the steady vortex flow patterns induced in the chamber is presented in Fig. 6 for various jet-to-disk separation distances. The results in Fig. 6(a) and (b) indicate that at the small H of 10.0 and 15.0 mm the inertia- and buoyancy-driven rolls are widely separated in the radial direction from each other since they are all relatively small. At this small H an increase in ΔT still causes the buoyancy roll to become bigger and stronger. But the inertia rolls are insensitive to the change in ΔT. Now as H is increased to 20.0 mm, the size growth of the primary inertia-driven roll with ΔT is clearly seen (Fig. 6 (c)). Meanwhile, the growth of the buoyancy roll with ΔT weakens the secondary inertia-driven roll. In fact, at $\Delta T = 25.0$ °C the secondary inertia-driven roll does not exist in the chamber. It is worth to note from Fig. 6(d) that at an even larger H of 30.0 mm the size growth of the buoyancy roll with ΔT results in the accompany-

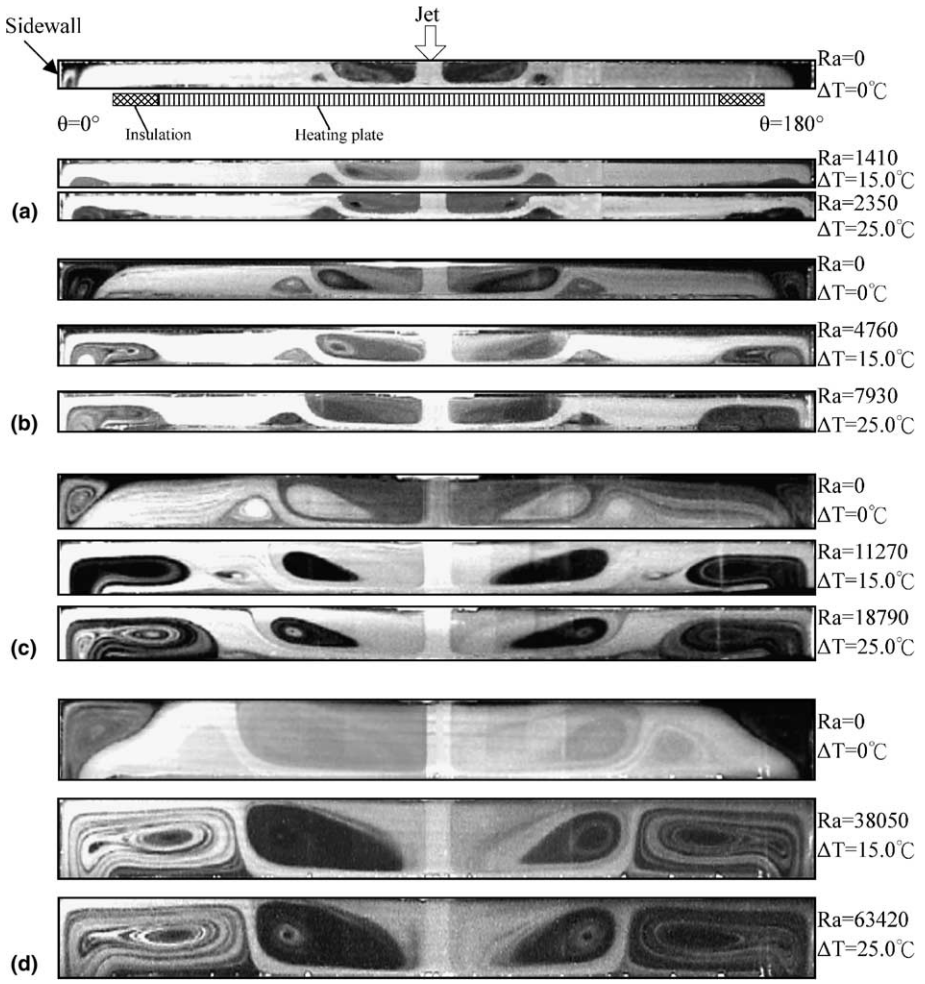

Fig. 6. Steady side view flow photos taken at the cross plane $\theta = 0°$ and 180° for various ΔT for $D_j = 10.0$ mm and $Q_j = 3.0$ slpm ($Re_j = 406$) with (a) $H = 10.0$ mm, (b) $H = 15.0$ mm, (c) $H = 20.0$ mm and (d) $H = 30.0$ mm.

ing slight decay of the primary inertia-driven roll since it is squeezed by the buoyancy-driven roll.

To reveal the complete picture of the vortex flow structure, the top view flow photos taken at the middle horizontal plane right between the chamber top and heated disk at $Z = 0.5$ for various jet-to-disk separation distances at given ΔT are presented in Fig. 7. The results clearly show the circular structure of the rolls and the primary inertia-driven roll grows in size when the jet-to-disk separation distance increases from 10.0 to 30.0 mm. Moreover, the secondary inertia-driven roll is distinctly observed in Fig. 7(c). In fact, for $D_j = 10.0$ mm and $Ra = 0$ the secondary inertia-driven roll appears in the processing chamber for various H at $Re_j > 270$. However, at small H of 10.0 mm the secondary inertia-driven roll can not be seen from the top view flow photo since the roll is relatively small and its height does not exceed the middle horizontal plane. Besides, we also note that the buoyancy-driven roll dominated in the outer region of the processing chamber increases in size with the jet-to-disk separation distance.

3.3. Size and location of the vortex rolls

To quantify the steady vortex flow characteristics we measure the maximum radial extent of the primary inertia-driven roll S_I, the maximum height of the outer buoyancy-driven roll S_O, and the radial location of the center of the secondary inertia-driven roll r_s from the steady side view flow photos. The results clearly indicate that for both injection pipes and for $H \leqslant 20.0$ mm S_I increases almost linearly with the jet Reynolds number for a given Ra. However, S_O decreases with an increase in Re_j. A close inspection of the data reveals that at the small H of 10.0 mm the increase of S_I with Re_j is substantially larger. To facilitate the flow design in the

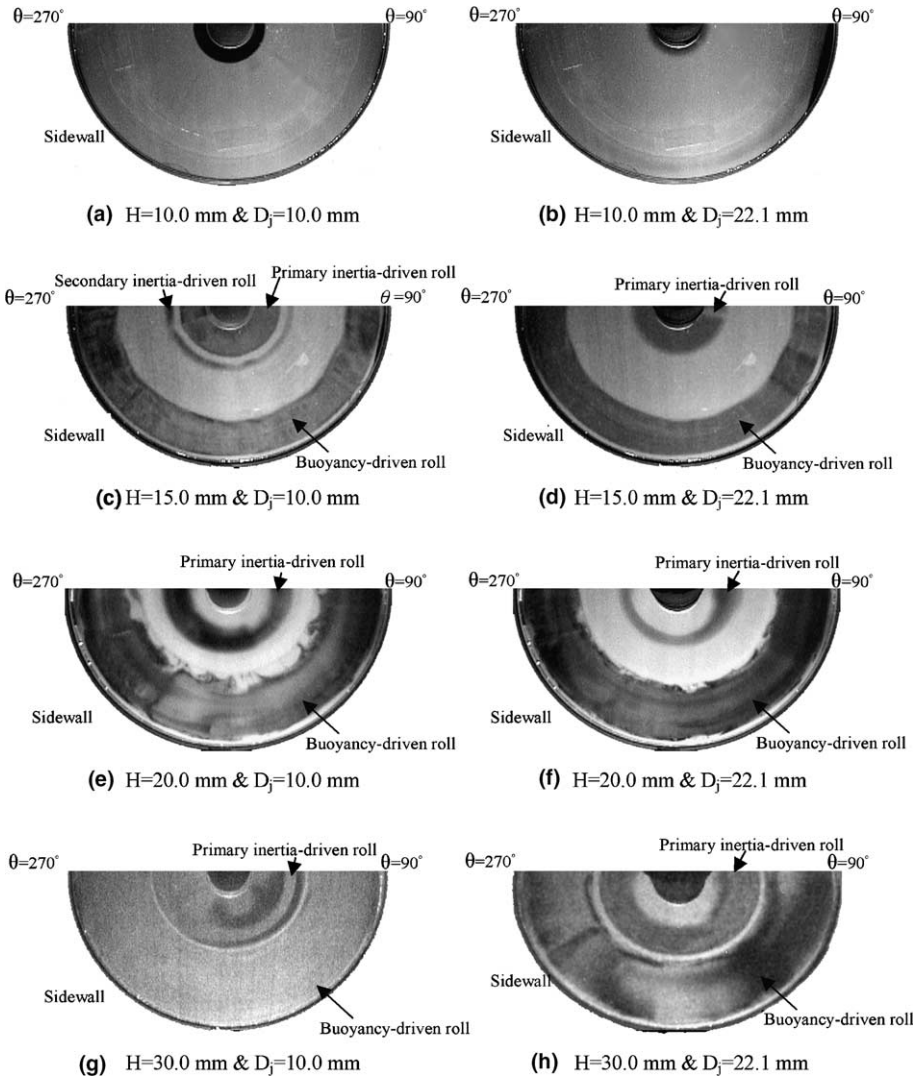

Fig. 7. Steady top view flow photos taken at the middle horizontal plane between the chamber top and heated disk with $Q_j = 3.0$ slpm ($Re_j = 406$ for $D_j = 10.0$ mm and $Re_j = 184$ for $D_j = 22.1$ mm) for (a) and (b) $Ra = 2350$, (c) and (d) $Ra = 6340$, (e) and (f) $Ra = 18{,}790$, and (g) and (h) $Ra = 63{,}420$.

practical application, empirical equations are proposed to correlate the data obtained here and those in the previous study [5]. They can be expressed as

$$\frac{S_I}{H} = 1.852 + 7.287 \times 10^{-5} Ra + 0.00229 Re_j \quad (4)$$

for $0 \leqslant Ra \leqslant 18,790$ and $61 \leqslant Re_j \leqslant 676$;

$$\frac{S_O}{H} = 0.0433 + 0.00444 Ra^{0.5} + 3.445 Re_j^{-0.5} \quad (5)$$

for $470 \leqslant Ra \leqslant 18,790$ and $61 \leqslant Re_j \leqslant 676$;

$$\frac{r_s}{D_j} = 3.283 + 0.000205 Ra + 0.00316 Re_j \quad (6)$$

for $0 \leqslant Ra \leqslant 7927$ and $270 \leqslant Re_j \leqslant 676$.

When compared with the present data, the standard deviations of Eqs. (4)–(6) are, respectively, 12%, 13% and 12%.

3.4. Temperature distributions in vortex flow

In addition to the vortex flow characteristics presented above, selected non-dimensional steady radial air temperature distributions in the vortex flow are measured along the line $\theta = 0°$ at the middle horizontal plane between the disk and chamber top. The data are shown in Fig. 8 along with the corresponding side view flow photos for $Q_j = 3.0$ slpm for various H. The non-dimensional air temperature Φ is defined as

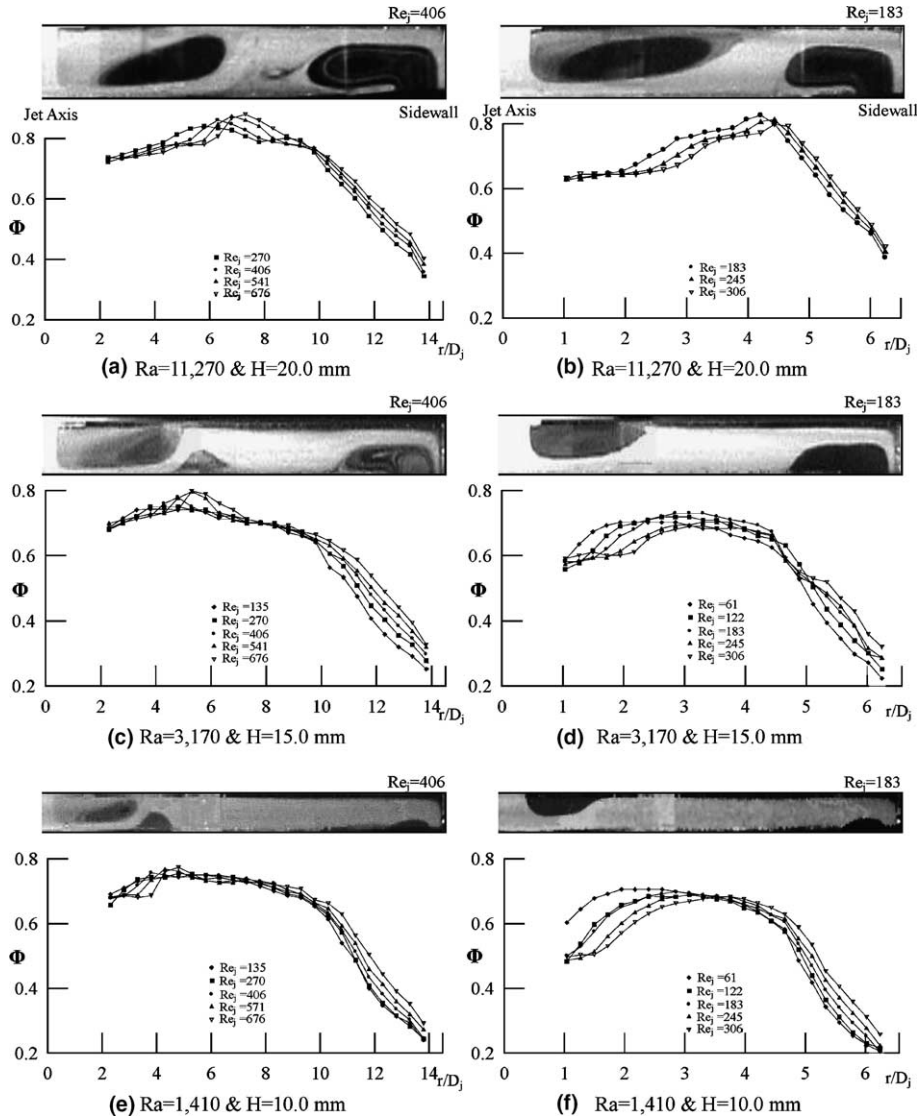

Fig. 8. Steady radial variations of non-dimensional air temperature for various Re_j along the line $\theta = 0°$ and $Z = 0.5$ at $\Delta T = 15.0\,°C$ and the corresponding selected side view flow photos at $\theta = 0°$ for $Q_j = 3.0$ slpm for H and D_j = (a) 20.0 and 10.0 mm, (b) 20.0 and 22.1 mm, (c) 15.0 and 10.0 mm, (d) 15.0 and 22.1 mm, (e) 10.0 and 10.0 mm, and (f) 10.0 and 22.1 mm.

$(T - T_j)/(T_f - T_j)$. Note that in the region dominated by the primary inertia-driven roll the air temperature increases with the radial distance measured from the jet axis. The air temperature reaches a maximum in the region when the wall-jet separates from the disk surface and moves obliquely upwards. Beyond that the air temperature starts to decline. Near the chamber side the temperature decline is relatively sharp due to the presence of the buoyancy-driven roll. Moreover, a sharper temperature decline results at a lower Re_j for given ΔT due to the stronger buoyancy roll. We also note that for a smaller jet-to-disk separation distance the air temperature in the middle horizontal plane is slightly lower. This is considered to result from the higher mean radial flow speed in the wall-jet region in the chamber with a smaller H for a given Q_j, which in turn causes weaker inertia-driven and buoyancy-driven rolls. Thus the above non-monotonic radial air temperature distributions for a given H result directly from the presence of the counter-rotating primary inertia-driven and buoyancy-driven vortex rolls in the chamber and the deflection of the impinging jet flow by these rolls. A close examination of these data further reveals that at increasing jet Reynolds number the temperature peak moves

away from the jet axis and the temperature decay in the region near the chamber side is small, reflecting the fact that we have a larger primary inertia-driven roll and a weaker buoyancy-driven roll for a higher Re_j.

4. Concluding remarks

Combined flow visualization and temperature measurement have been conducted here to explore how the jet-to-disk separation distance affects various aspects of the steady vortex flow resulting from a mixed convective low speed air jet impinging onto a heated horizontal disk confined in a vertical cylindrical chamber. Major results obtained are briefly summarized in the following:

1. A tertiary inertia-driven circular vortex roll is first identified in the confined impinging jet as the jet Reynolds number is high enough. The tertiary roll is relatively small compared with primary inertia-driven roll. Beyond this Re_j the high jet inertia causes the vortex flow to become time dependent.
2. The critical jet Reynolds numbers for the onset of the primary, secondary and tertiary inertia-driven rolls increase noticeably when H is reduced from 20.0 to 10.0 mm. But the corresponding critical jet Reynolds numbers for the tertiary inertia-driven roll do not change for a reduction of H from 30.0 to 20.0 mm.
3. A reduction in H results in a significant decrease in the Rayleigh number since $Ra \propto H^3$ and can substantially reduce the size and strength of the buoyancy-driven roll. The present data of the critical condition for the onset of the buoyancy-driven roll can be approximately expressed as the local buoyancy-to-inertia ratio at the edge of the disk $Gr/Re_{we}^2 \approx 33.0$.
4. Both the inertia- and buoyancy-driven vortex rolls grow in size and intensity for an increase in the jet-to-disk separation distance. At $H = 30.0$ mm the primary inertia-driven and the buoyancy-driven rolls both become so large and they contact with each other. Thus no space is left for the secondary inertia-driven roll to appear.
5. The non-monotonic radial air temperature distribution in the flow mainly reflects the counter-rotating vortex flow structure of the primary inertia-driven and buoyancy-driven rolls.
6. The empirical equations are proposed to correlate the size of the primary inertia- and buoyancy-driven rolls and the location of the secondary inertia-driven roll.

Acknowledgment

The financial support of this study by the engineering division of National Science Council of Taiwan, ROC through the contract NSC90-2212-E-009-059 is greatly appreciated.

References

[1] S. Polat, B. Huang, A.S. Mujumdar, W.J.M. Douglas, Numerical flow and heat transfer under impinging jets: a review, in: C.L. Tien and T.C. Chawla (Eds.), Annular Review of Numerical Fluid Mechanics and Heat Transfer, vol. 2, Hemisphere, Washington, D.C., 1989, pp. 157–197.
[2] G.B. Stringfellow, Organometallic Vapor Phase Epitaxy: Theory and Practice, Academic Press, San Diego, 1989 (Chapter 5).
[3] S.A. Campbell, The Science and Engineering of Microelectronic Fabrication, Oxford University Press, New York, 1996 (Chapter 6).
[4] M.L. Hitchamn, K.F. Jensen, Chemical Vapor Deposition (Principle and Application), Academic Press, San Diego, 1993 (Chapter 2).
[5] J.C. Hsieh, T.C. Cheng, T.F. Lin, Characteristics of vortex flow in a low speed air jet impinging onto a heated disk in a vertical cylindrical chamber, International Journal of Heat and Mass Transfer 46 (2003) 4639–4656.
[6] M.T. Scholtz, O. Trass, Mass transfer in a nonuniform impinging jet, AIChE Journal 16 (1970) 82–96.
[7] E.M. Sparrow, T.C. Wong, Impingment transfer coefficients due to initially laminar slot jets, International Journal of Heat and Mass Transfer 18 (1975) 597–605.
[8] J.H. Masliyah, T.T. Nguyen, Mass transfer due to an impinging slot jet, International Journal of Heat and Mass Transfer 22 (1979) 237–244.
[9] P. Hrycak, Heat transfer from round impinging jets to a flat plate, International Journal of Heat and Mass Transfer 26 (1981) 1857–1865.
[10] N.R. Saad, W.J.M. Douglas, A.S. Mujumdar, Prediction of heat transfer under an axisymmetric laminar impinging jet, Industrial and Engineering Chemistry Research Fundamentals 16 (1977) 148–154.
[11] H.S. Law, J.H. Masliyah, Mass transfer due to a confined laminar impinging axisymmetric jet, Industrial and Engineering Chemistry Research Fundamentals 23 (1984) 446–454.
[12] L.P. Chua, S.C.M. Yu, H.-S. Li, Flow visualization and preliminary measurements of a confined jet with and without target, International Communications in Heat and Mass Transfer 27 (2000) 191–200.
[13] P.R. Voke, S. Gao, Numerical study of heat transfer from an impinging jet, International Journal of Heat and Mass Transfer 41 (1998) 671–680.
[14] J.A. Fitzgerald, S.V. Garimella, A study of the flow field of a confined and submerged impinging jet, International Journal of Heat and Mass Transfer 41 (1998) 1025–1034.
[15] T.H. Park, H.G. Choi, J.Y. Yoo, S.J. Kim, Streamline upwind numerical simulation of two-dimensional confined impinging slot jets, International Journal of Heat and Mass Transfer 46 (2003) 251–262.
[16] H.S. Law, J.H. Masliyah, Numerical prediction of the flow field due to a confined laminar two-dimensional submerged jet, Computers and Fluids 12 (1984) 199–215.

[17] V.A. Chiriac, A. Ortega, A numerical study of the unsteady flow and heat transfer in a transitional confined slot jet impinging on an isothermal surface, International Journal of Heat and Mass Transfer 45 (2002) 1237–1248.
[18] R. Viskanta, Heat transfer to impinging isothermal gas and flame jets, Experimental Thermal and Fluid Science 6 (1993) 111–134.
[19] K. Jambunathan, E. Lai, M.A. Moss, B.L. Button, A review of heat transfer data for single circular jet impingement, International Journal of Heat and Fluid Flow 13 (1992) 106–115.
[20] G. Wahl, Hydrodynamic description of CVD processes, Thin Solid Films 40 (1977) 13–26.
[21] A.H. Dilawari, J. Szekely, A mathematical representation of a modified stagnation flow reactor for MOCVD application, Journal of Crystal Growth 108 (1991) 491–498.
[22] P.N. Gadgil, Optimization of a stagnation point flow reactor design for metalorganic chemical vapor deposition by flow visualization, Journal of Crystal Growth 134 (1993) 302–312.
[23] H.V. Santen, C.R. Kleijn, H.E.A. Van Den Akker, Symmetry breaking in a stagnation-flow CVD reactor, Journal of Crystal Growth 212 (2000) 311–323.
[24] S.J. Kline, F.A. McClintock, Describing uncertainties in single-sample experiment, Mechanical Engineering 75 (1953) 3–8.